Materials Today • Volume xxx, Number xx • xxxx 2021 RESEARCH

ELSEVIER

RESEARCH: Original Research

Hollow-grained "Voronoi foam" ceramics with high strength and thermal superinsulation up to 1400 °C

Sa Li [1,2], Chang-An Wang [1,*], Fuqian Yang [3], Linan An [4,*], Kangpyo So [5], Ju Li [5,*]

[1] State Key Lab of New Ceramics and Fine Processing, School of Materials Science and Engineering, Tsinghua University, Beijing 100084, China
[2] School of Materials Science and Engineering, Tongji University, Shanghai 201804, China
[3] Department of Chemical and Material Engineering, University of Kentucky, Lexington, KY 40506, USA
[4] Department of Materials Science and Engineering, Advanced Materials Processing and Analysis Center, University of Central Florida, Orlando, FL 32816, USA
[5] Department of Nuclear Science and Engineering and Department of Materials Science and Engineering, Massachusetts Institute of Technology, Cambridge, Massachusetts 02139, USA

Nanostructures tend to be unstable at high temperatures due to large capillary energies, and therefore nanotechnology has not yet found many high-temperature applications at 1000 °C and above. By taking advantage of the high-temperature stability of refractory ceramics, here we develop a new approach of making hollow nano-grained materials to achieve thermal superinsulation across a wide temperature range, where the gaseous voids are mostly isolated within individual grain, with size comparable to the mean free path of air molecules to lower the thermal conduction by Knudsen effect. We have proved this general concept with hollow-grained $La_2Zr_2O_7$ ceramic, and demonstrated exceptionally low thermal conductivity (0.016 W/(m·K)), the lowest ever reported for hard materials at or above room temperature. The centimeter-scale samples also have ultrahigh compressive strength (251 MPa), tensile strength in bending up to 100 MPa, and excellent thermal stability up to 1400 °C in air, due to monodispersity of pores that delays coarsening.

Introduction

Crystalline ceramic nanowires (1D) and nanoshells (2D) can be surprisingly robust mechanically in bending, and even stretching. If properly assembled into closed-cell foams or open-cell nanolattices, the 3D assembly could possess a satisfactory level of flaw tolerance [1] and structural integrity seen in some ceramic nanolattices [2], with distinctly different macro-properties from the monolith [3]. Porous materials design by judiciously controlling the air pore topology and geometry could change the effective properties of a macroscopic solid by several orders of magnitude [4]. In particular, it has been shown that the thermal conduction properties can vary greatly by tailoring the porous architecture in terms of porosity (ranging from a few to >95vol %), pore size (from several nanometers to millimeters), shape, interconnectivity and distribution of pores, and so on, all of which are strongly influenced by the manufacturing method [3]. For example, bulk hollow micro-/nanostructures have been synthesized by hard/soft/sacrificial templating [5,6], and has been used for enhancing thermal insulation [7], wherein cavity size reduction to about $\leq$ 350 nm led to a marked decrease in the effective thermal conductivity. However, in order to achieve ultralow thermal conductivity, a high porosity, i.e. low density, is usually required, which often leads to poor mechanical integrity. Fortunately, the mechanical degradation could be largely slowed down if appropriately designing material's microarchitecture [8]. In this work, we exercise such design freedom on $La_2Zr_2O_7$ (LZO), a refractory ceramics with lower bulk thermal conductivity and better thermal stability than yttria-stabilized zirconia (YSZ) [9]. We show that the effective thermal conductivity can be reduced by another *two orders of magnitude* while maintaining satisfactory strength characteristics as a hard material, in

* Corresponding authors.
E-mail addresses: Wang, C.-A. (wangca@tsinghua.edu.cn), An, L. (Linan.An@ucf.edu), Li, J. (liju@mit.edu).

 https://doi.org/10.1016/j.mattod.2021.02.003

Please cite this article in press as: S. Li et al., Materials Today (2021), https://doi.org/10.1016/j.mattod.2021.02.003

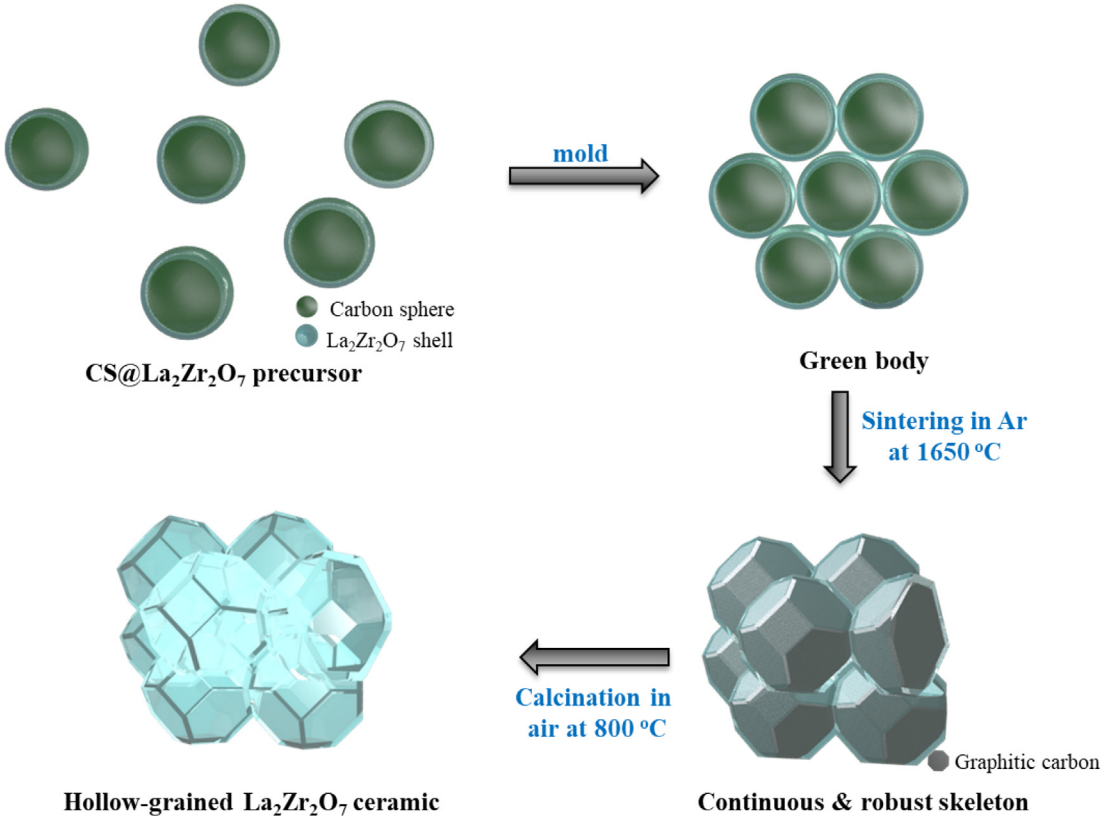

FIGURE 1

Material processing. Schematic of the two-step sintering process developed in this study.

a well-designed hollow-grained polycrystal that we call "Voronoi foam", with potential application as thermal barrier coating [10] in erosive or other mechanically/chemically demanding conditions, or as free-standing film for thermal insulation in high-temperature MEMS/NEMS devices. The synthesis strategy we present is general and can be applied to many crystalline ceramic materials.

As LZO has excellent thermal stability in air and thermal shock resistance [9], our goal is to design a thermal superinsulator out of it in a very wide temperature range. A thermal superinsulator has thermal conductivity $\lambda < \lambda_{air} = 0.026$ W/(m·K) (diffusive only, without convective heat transfer). Monolithic LZO has λ 1.5–2 W/(m·K) in the wide temperature range between 200–1500 °C [9], already close to the minimum thermal conductivity of 1.4 W/(m·K) [11] for dense solid based on Einstein's fundamental derivation [12]. We are thus constrained by the following considerations in order to induce thermal superinsulation across a wide temperature range, where the effective λ of the ceramic/air composite must be less than that of either the ceramic or the free air:

i) The volume fraction of the LZO phase (ϕ_{ceram}) must be low enough because heat conduction through percolating LZO ligaments is much faster than in air.
ii) However, ϕ_{ceram} cannot be too low due to the mechanical robustness requirement for the coating or free-standing film in erosive or other mechanically demanding environments [10].
iii) Because the mean free path of air molecules in free air is ~70 nm at ambient pressure [13], the pore diameter D must be nanoscopic in order for the mean-free path of air molecules to be dimensionally confined (Knudsen effect [14]), to achieve thermal conductivity less than free air.
iv) On the other hand, hollow nanostructures are thermodynamically unstable [15]. High-temperature aging drives thermal vacancies emission and coarsening of the pores, and eventual consolidation. To delay the consolidation of pores at temperature up to 1500 °C, D cannot be too small.

Aerogels, while achieving thermal superinsulation, are situated in a completely different materials parameter space, with much lower ϕ_{ceram} and much smaller D. They are much softer and weaker mechanically, with Young's modulus in the MPa range, and do not qualify as hard material. They have huge internal surface area (500–1500 m^2/g) and capillary energy density, so generally become thermally unstable and consolidate above 700 °C. Also, structurally speaking, aerogels are more like open-cell lattices with 1D chains, whereas our material is much closer to closed-cell foams with high-quality single-crystalline walls, giving much lower fluid permeability across the sample, thus stopping the penetration of corrosive agents. Our hollow-grained structure is akin to Voronoi partition of 3D space, with the partition centers at the origin of spherical pore in each grain, and thus we call this structure "Voronoi Nanofoam" (Fig. 1). To delay coarsening, the pores need to be highly monodisperse, enabling thermal stability up to 1400 °C.

Please cite this article in press as: S. Li et al., Materials Today (2021), https://doi.org/10.1016/j.mattod.2021.02.003

Results and discussion

In this study, the sacrificial templating method is used and the synthesis method is schematically illustrated in Fig. 1. First, highly monodisperse carbon spheres (CSs) are synthesized and used as the templates. The CSs are then coated with $La_2Zr_2O_7$ by immersing them in a liquid precursor to form CS-$La_2Zr_2O_7$ core–shell nanopowder. Subsequently, the core–shell powder is sintered to dense ceramics in a protective atmosphere. Finally, the ceramics are heat-treated in air to remove the carbon cores to form the hollow-grained structure. This method provides flexibility to tailor the pore size (by varying the size of the CSs) and wall thickness (by varying the thickness of the $La_2Zr_2O_7$ coating layer) independently for optimizing the properties.

A hydrothermal process was adopted to synthesize the CSs, which can produce a large quantity of monodispersed CSs [16]. Fig. 2a and 2b are typical SEM and TEM images of the as-synthesized carbon spheres, respectively. It is seen that the CSs exhibit perfectly spherical shape with a very uniform size of $D \sim 240$ nm. Such CSs were then coated with $La_2Zr_2O_7$ precursor by immersing them into a solution containing $La(NO_3)_3$ and $ZrOCl_2$. SEM image of the CSs after coating (Fig. 2c) reveals that the surface of the coated spheres becomes rough, indicating the presence of the coating, while the powders still have a well-defined spherical shape and excellent mono-dispersity. TEM observation (Fig. 2d) shows an obvious contrast between the edge and center of the coated powders. EDS analysis (Fig. S1) reveals that there is a much higher amount of La and Zr around the edge area than in the center, confirming the presence of the coating on the surface. Close observations of more than ten spheres suggest that the coating layer is dense and completely covers the CSs. By controlling the immersion time, the core–shell powders with different coating thicknesses were synthesized as shown in Table 1.

The coated powder was then compressed into green compacts, which were sintered at 1650 °C for 2 h in argon protection. This densifies the ceramic skeleton while it was still supported by the CS template. The sintered samples were then calcined in air at 800 °C for 12 h to remove the CSs templates and form hollow-grained structure. XRD and Raman analyses (Fig. S2) revealed that the resultant hollow-grained ceramics was a single-phased crystalline $La_2Zr_2O_7$ with cubic Fd-3 m space group [17]. No trace of carbon was detected, which suggests the complete removal of the inner carbon. The microstructure of the hollow-grained ceramics was analyzed using electron microscopy. Fig. 3a shows an SEM image of the fracture surface of the material. It is seen that the ceramic skeleton was sintered to almost full density, with faceted polyhedral grains and uniform grain size of ~200 nm.

The tetrakaidecahedron grains were obviously transformed from the spherical starting particles during sintering. The

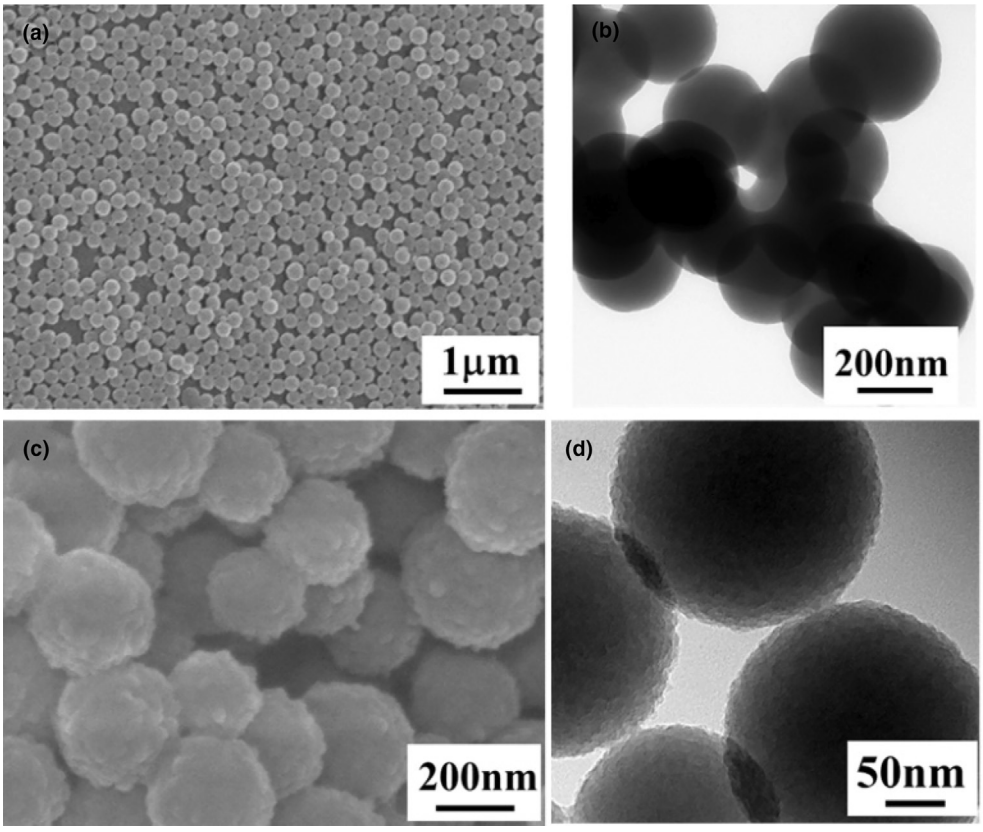

FIGURE 2

Characterizations of precursors. a) SEM and b) TEM images of as-obtained carbon spheres from hydrothermal method; c) SEM and d) TEM images of $La_2Zr_2O_7$-carbon hybrid composites after coating.

Please cite this article in press as: S. Li et al., Materials Today (2021), https://doi.org/10.1016/j.mattod.2021.02.003

TABLE 1

Thermal and mechanical properties of the hollow-grained $La_2Zr_2O_7$ ceramics with different shell thicknesses and the solid $La_2Zr_2O_7$ counterpart.

Shell thickness (nm)	ρ (g/cm^3)	Porosity (%)	λ^* (W/(K·m))	σ_f (MPa)	σ_f/λ^*
20	0.71	88.2	0.016	101.4 ± 1.3	6337.5
30	1.23	79.5	0.020	157.7 ± 4.5	7885.0
40	1.47	75.6	0.022	228.2 ± 7.5	10372.7
50	1.86	69.1	0.025	259.1 ± 9.7	10364.0
Pure $La_2Zr_2O_7$	6.014	/	1.900	518.8	185.3

λ^* is the room-temperature thermal conductivity.
σ_f is the compressive strength.

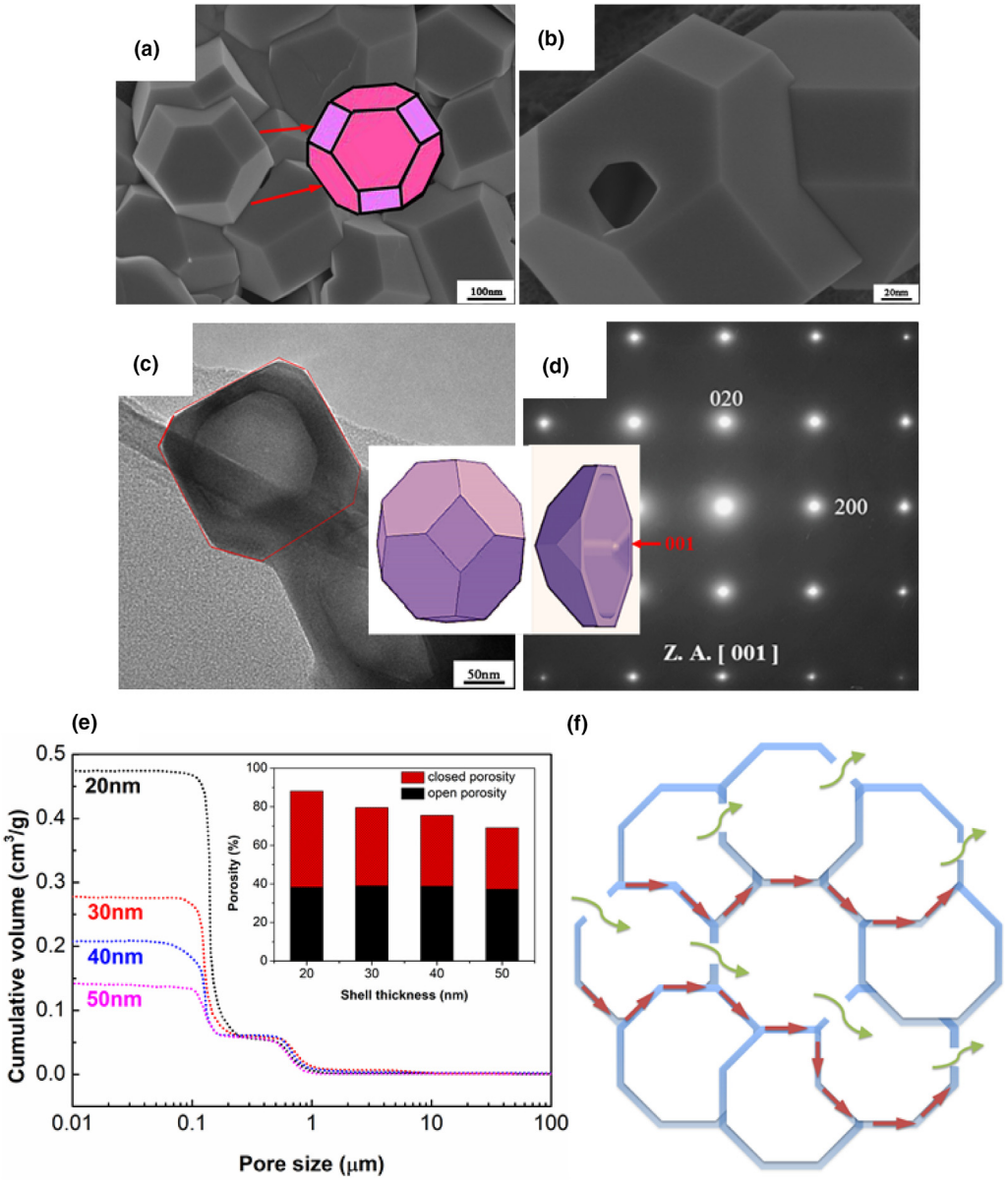

FIGURE. 3

Microstructures of hollow-grained $La_2Zr_2O_7$ ceramics. a) Panoramic and b) high-magnified SEM image of the cross section after calcined in air at 800 °C for 12 h; c) TEM image and d) corresponding SEAD pattern of the bulk. The insert represents a tetrakaidecahedron model; e) mercury intrusion results demonstrating the porosity distribution and the inset stacked column chart reveals the closed porosity and open porosity; f) illustration of heat transfer paths where the blue skeleton represents LZO shell, green arrows show heat transfer through gas phase and wine arrows indicate heat transfer through LZO phase.

Please cite this article in press as: S. Li et al., Materials Today (2021), https://doi.org/10.1016/j.mattod.2021.02.003

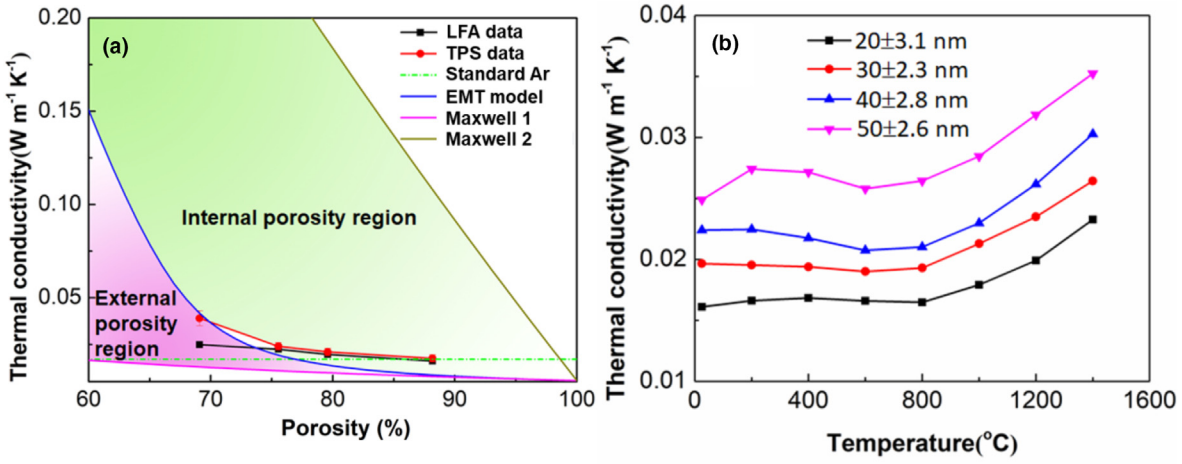

FIGURE. 4

Thermal performance of hollow-grained $La_2Zr_2O_7$ ceramics. a) Comparison of thermal conductivities measure experimentally through LFA and TPS with predicted values from the thermal conductivity bounds proposed by ME and EMT models; b) thermal conductivity of $La_2Zr_2O_7$ ceramics at various temperatures.

mono-dispersity and the spherical shape of the starting particles likely facilitated such a transformation, with very little coarsening in the process. It is also seen (Fig. 3a) that the fracture was almost intergranular, suggesting the grain is stronger than the grain boundary, even though the wall of the ceramic skeleton was only a few tens of nanometers. From the broken grains (Fig. 3b), it is obvious that the tetrakaidecahedron grains have a hollow structure. The hollow nature of the $La_2Zr_2O_7$ grains can be seen more clearly from the TEM image (Fig. 3c), which reveals that the grain had a tetrakaidecahedron outer shape and nearly spherical inner cavity (see insert in Fig. 3c). The thickness of the ceramic wall was about 20–30 nm. From the SAED pattern in Fig. 3d, a pure LZO cubic diffraction is observed, with no presence of any other atoms, also indicating carbon is completely eliminated after two-step sintering (Fig. 1). Mercury intrusion measurement was used to determine the size distribution of the open pores, and as shown in Fig. 3e, some open pores with a size of 0.6 μm as well as a large fraction of 140 nm open pores that are originated from the inner voids of the hollow grains (as compared to Fig. S3), were detected. Furthermore, the open porosity of the samples was measured using the Archimedes' method with distilled water as the immersion medium, and the results can be found in the inset of Fig. 3e. It seems for samples with different shell thickness, the open porosity is similar, at around 40%. Previous researches reveal that for porous ceramics, the gas phase has a physical percolation threshold at the porosity value of ~30% [18] and mechanical percolation threshold of 20% porosity [19], both of which, however, are not necessarily the critical porosity from a heat transfer perspective. As a matter of fact, with such a moderate porosity in this study, it seems the gas phase and ceramic phase could be locally continuous and form heat transfer pathways, as illustrated in Fig. 3f.

The density of the sintered ceramics was measured using the Archimedes method and listed in Table 1. The ceramics exhibited a high porosity (ϕ_{ceram} as low as 11.8 %) even though the skeleton was sintered together. The Voronoi foam structure is stable in air in the temperature range of 25–1400 °C, and the high-temperature shrinkage is especially evaluated in Fig. S4. After samples treated at 1400 °C for 2 h, negligible linear shrinkage is observed, confirming the high-temperature stability. Its thermal diffusivity was measured using laser-flash method. The thermal conductivity (λ) was then calculated and listed in Table 1, using the following equation:

$$\lambda = C_p(T) \times \alpha(T) \times \rho(T) \quad (1)$$

where $C_p(T)$ is the specific heat capacity of $La_2Zr_2O_7$ obtained from the literature, $\alpha(T)$ is the thermal diffusivity, and $\rho(T)$ is the density of the material. Note that the slight decrease in the density due to thermal expansion is neglected, and $\rho(T) \equiv 6.014\ g/cm^3$ is adopted in this study. On the other hand, a modified model of $C_p(T)$ is proposed in Fig. S5, where the heat capacity of $La_2Zr_2O_7$ at various temperature can be estimated by $C_p(T) = 0.456 + 0.0000523\ T - 6635\ T^{-2}$, and the specific heat capacity of LZO at 25–1400 °C that is used in Eq. (1) is listed in Table S1. The temperature dependence of thermal diffusivity is determined from transient temperature versus time curves, and a typical measurement along with its fit is provided in Fig. S6. To take thermal radiative heat loss into consideration, instead of the conventional half-rise-time method, Cape-Lehmann-model [20], which maintains a non-linear regression with consideration of radial and facial heat losses, is used to fit the transient temperature history curve obtained by the laser flash [21]. It is seen that all obtained ceramics had extremely low thermal conductivity, which are about two orders of magnitude lower than that of the bulk counterpart and even lower than that of air (0.026 W/(m·K)) [22]. The thermal conductivity of the ceramics decreases with decreasing the thickness of the shell. The sample with a shell thickness of 20 nm has thermal conductivity as low as ~0.016 W/(m·K), which is the lowest value that has ever been reported for hard materials. As double-check, we also utilize a transient plane source method (TPS) to measure the thermal conductivity from 25 °C to 500 °C and compare the measured values with LFA results in Fig. S7. Some discrepancy could be observed, most of which is on the 10^{-3} W/(m·K) order of magnitude, except the 50 nm sam-

Please cite this article in press as: S. Li et al., Materials Today (2021), https://doi.org/10.1016/j.mattod.2021.02.003

ple tested at 25 °C where TPS measurement is 0.014 W/(m·K) higher than that from LFA measurement. Because estimation of the thermal conductivity through LFA requires additional knowledge of other relevant properties, such as thermal diffusivity, specific heat, density, and sample thickness. Errors in the measurement of these additional parameters are propagated through data reduction and result in error in the thermal conductivity determination.

In Supporting Information (SI), we modeled the measured conductivity bounds by the Maxwell-Eucken (ME) and Effective Medium Theory (EMT) models, where the Knudsen effect [14] on gaseous thermal conductivity (Ar gas is assumed here because different gases seem to have negligible influence (<0.01 W(m·K)) on the overall thermal conductivity, as revealed in Fig. S10 and Table S2) in confined pores is taken into consideration. Fig. 4a compares the thermal conductivity measured experimentally (both LFA and TPS) with those proposed thermal conductivity bounds. While EMT model well predicts the thermal conductivity of samples with 50 nm-thick nanoshells, some deviation can be seen in the thermal conductivities of samples with smaller shell thickness. Previously, the effective thermal conductivity region bounded by the Hashin-Shtrikman model [23] could be divided into external porosity and internal porosity regions by the EMT equation [24]. To be specific, external porosity is identified as that in which the gaseous component forms continuous conduction pathways and internal porosity is that in which the condensed phase forms continuous conduction pathways. Apparently, for samples with a shell thickness of 20–40 nm, the effective thermal conductivities lay within the "internal porosity region", indicating the majority of the heat transfer is through the condensed phase, namely the LZO skeleton.

The thermal conductivity and stability of the hollow grained $La_2Zr_2O_7$ ceramics were tested from 25 °C to 1400 °C. As shown in Fig. 4b, the thermal conductivity of $La_2Zr_2O_7$ decreases gradually with increasing temperature up to 800 °C, and then increases slowly with further increasing temperatures. We think the nonmonotonic temperature dependences of thermal conductivity are caused by a combined action of three mechanisms: (a) solid state thermal conductivity (λ_s), (b) gas thermal conductivity (λ_g), and (c) radiation thermal conductivity (λ_r). For crystalline LZO, λ_s generally follows the $1/T$ law and decrease with T [25], while at high temperature, where the phonon mean free path is comparable to the crystal lattice size, λ_s almost maintains constant and does not change with T. Regarding gas thermal conductivity, as will discussed in SI, its relationship with T could be expressed as $\frac{0.017}{1+0.00676T}$, exhibiting a monotonical decrease with T. Therefore, in the low-temperature range, λ_g and λ_s, both of which exhibit a decreasing trend with temperature enhancement, dominate and add up together to contribute the measured thermal conductivity, whereas thermal radiation conductivity calculated by $\frac{16n^2\sigma T^3}{3\alpha}$ [26], where n is the refractive index and α is the mean absorption coefficient of LZO, monotonically increases with T starts to be competitive at certain high temperature (we guess from 800 °C in this study). Therefore, the overall thermal conductivity exhibits a nonmonotonic temperature dependence. Similar temperature dependences of thermal conductivity have been obtained for Al_2O_3 hollow spheres tested in nitrogen [27]. Note that the Kapitza resistance of grain boundaries was not considered. According to a previous report about YSZ materials [28] that have similar thermal properties with LZO, the Kapitza resistance is temperature independent above room temperature, indicating the same temperature dependence for polycrystalline LZO bulk with nano-size grains. For our sample with a shell thickness of 20 nm, the thermal conductivity of 0.0126 W/(m·K) was achieved at 800 °C. This value is more than 100 times lower than the calculated amorphous limit of bulk LZO [11]. The very stable thermal conductivity at high tempera-

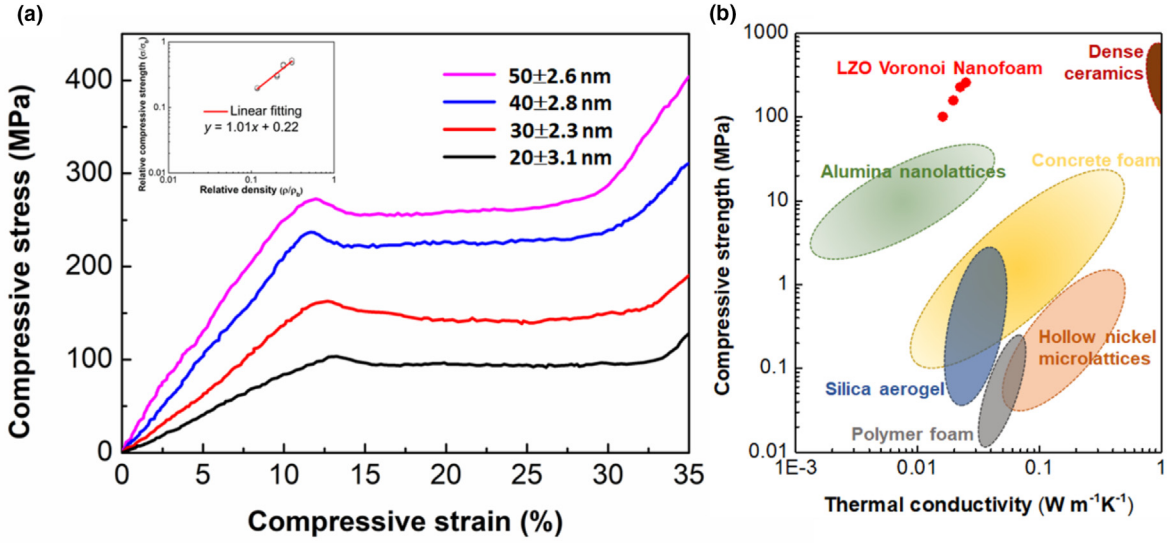

FIGURE. 5

Mechanical performance. a) Compressive strain–stress curves of the hollow grained $La_2Zr_2O_7$ specimens. The inset is relative compressive strength (σ/σ_b) plotted against relative density (ρ/ρ_b) on logarithmic scales for hollow LZO with different shell thickness; b) Ashby chart of compressive strength versus thermal conductivities. Here polymer foam [30], silica aerogel [31], hollow nickel microlattices [32], concrete foam [33], alumina nanolattices [2,34] and ceramics were compared with hollow LZO.

Please cite this article in press as: S. Li et al., Materials Today (2021), https://doi.org/10.1016/j.mattod.2021.02.003

tures up to 1400 °C also indicated that our hollow material exhibits excellent thermal stability (consistent with high-temperature shrinkage results in Fig. S4), despite the thermodynamic tendency to consolidate [15]. All these validate the success of our materials design strategy.

To characterize mechanical properties of the porous $La_2Zr_2O_7$ ceramics, compression tests were carried out on samples with different shell thicknesses, as well as the dense $La_2Zr_2O_7$ counterpart. Fig. 5a shows the representative compressive stress–strain curves. Unlike the dense counterpart, which exhibits a typical brittle fracture during compression, the hollow grained ceramics exhibited "pseudo-ductile" behavior. Compressive stress firstly increases with increasing strain, becomes constant, and then increases with increasing strain again. The increase in the stress after a long plateau corresponds to the initiation of local densification of the hollow-grained $La_2Zr_2O_7$ ceramics. Similar stress–strain curve behavior was reported by Ashby [4,29] and Greer et al. [2]. The compressive strain for all the samples of different shell thicknesses can reach 30–34% before the occurrence of densification, which indicates large damage tolerance [1] and load-bearing capacity. The compressive stress, i.e. the failure strength, of the hollow grained $La_2Zr_2O_7$ ceramics is listed in Table 1, which decreases from 259 to 101 MPa with decreasing shell thickness from 50 nm to 20 nm (shell thickness uncertainty is also measured in Fig. S8). An Ashby chart of compressive strength versus thermal conductivity that compares the polymer foam [30], silica aerogel [31], hollow nickel microlattices [32], concrete foam [33], alumina nanolattices [2,34] and ceramics with hollow LZO is plotted in Fig. 5b.

Furthermore, the measured values of the failure strength σ_f are fitted by a classic model of mechanical strength of cellular solid, which is generally expressed as a function of the density ρ [29]:

$$\frac{\sigma_f}{\sigma_{f,b}} = \beta\left(\frac{\rho}{\rho_b}\right)^m \tag{2}$$

where $\sigma_{f,b}$ is the fracture strength of the corresponding bulk materials. The constants of β and m depend on the structure of the cellular solid with $m = 3/2$ for bending-dominated behavior, and

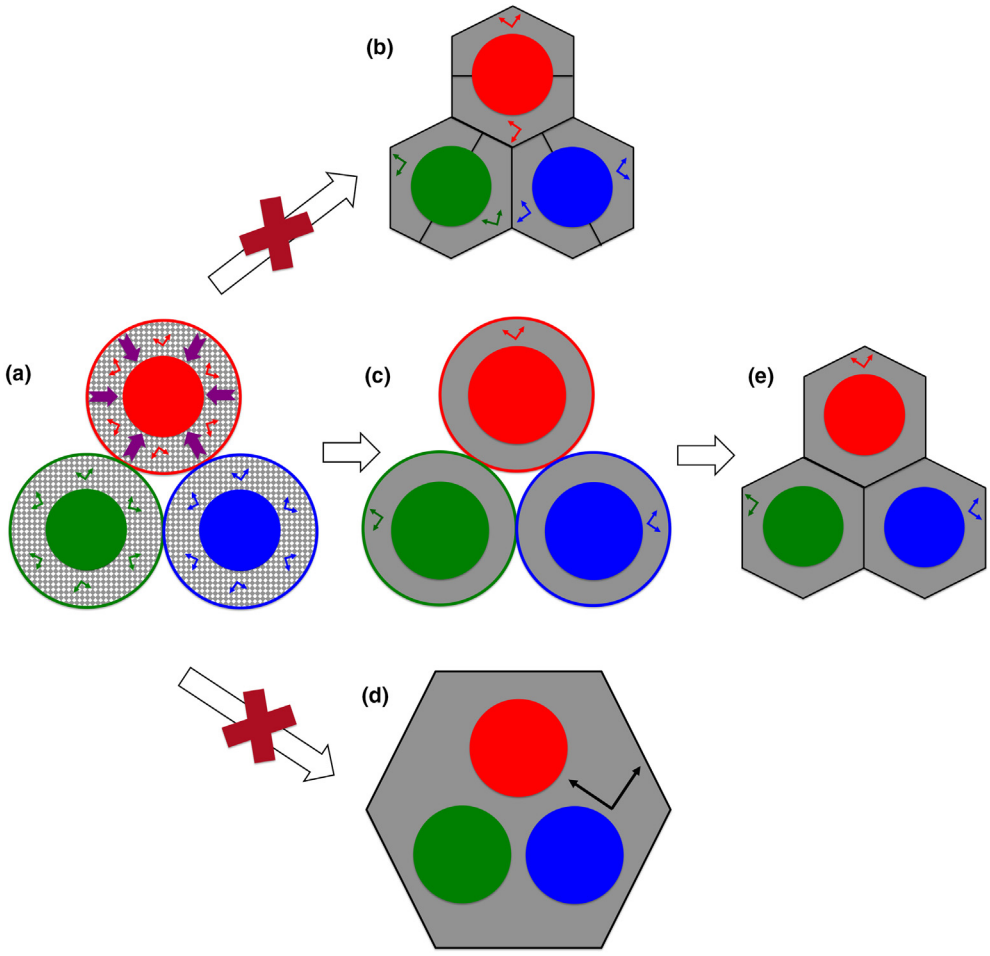

FIGURE. 6

The formation mechanism of the Voronoi Nanofoam structure. a) Green body before the 1650 °C sintering. Red, blue, green filled circles represent carbon spheres, and the micro-porous outer layers represent very small randomly oriented nanograins of ceramics. The unfilled circles represent "circle of influence", inside which grain coarsening is greatly expedited. b) Illustration of 1:2 arrangement, where one carbon sphere, surrounded by two grains). c) Formed 1:1 arrangements by the time the rough contact interfaces are eliminated completely. d) Illustration of 2:1 arrangement, where two carbon spheres, surrounded by one grain. e) Voronoi structure after sintering, with dense single crystal surrounding each carbon sphere. The orthogonal frames represent the grain lattice orientation, which is inherited from a single nanograin in (a), which has grown to surround one and only one carbon sphere completely.

Please cite this article in press as: S. Li et al., Materials Today (2021), https://doi.org/10.1016/j.mattod.2021.02.003

$m = 1$ for plastic stretch-dominated behavior [29]. Using the data in Table 1, one obtains $\beta = 0.22$ and $m = 1$ (inset of Fig. 5a). While conventional cellular foam materials with stochastic porosity are known to deform predominantly through bending of their cell walls/struts ($m = 1.5–2$), it seems our delicately designed Voronoi foam has a reduced coupling relationship between mechanical properties and mass density, exhibiting a slower degradation in mechanical properties as the density decreases.

Additionally, four-point bending test of the hollow grained $La_2Zr_2O_7$ ceramics was also performed (Fig. S5), in which a *tensile stress state* is sustained in half of the specimen. The peak *tensile* strength of the composite is measured to range from 100 to 50 MPa with decreasing shell thickness from 50 nm to 20 nm. This is extraordinary for a light ceramic foam, and is orders of magnitude larger than aerogels.

We would like to end by addressing a puzzling aspect of our process. The final Voronoi foam structure has excellent thermal stability against coarsening, due to the high degree of monodispersity of the grain and air pore sizes inside. Because each carbon sphere was initially coated with very small nanograins of ceramics with plenty of pores in between (Fig. 6a), it is reasonable to ask why and how during the 1650 °C sintering, these nanograins coarsen into a larger single-crystal grain that envelops the carbon sphere completely, so there is just one carbon sphere per grain (1:1), and not say, a 1:2 arrangement (one carbon sphere, surrounded by two grains, as illustrated in Fig. 6b), or 2:1 arrangement (two carbon spheres, surrounded by one grain, as illustrated in Fig. 6d), which are indeed rarely seen in electron microscopy of our material. Each carbon sphere appears to have its own "circle of influence" (red, blue and green circles in Fig. 6a) that facilitates grain coarsening inside, but not towards the outside of the circle, resulting in the eponymous Voronoi tessellation of space by dense crystals. It would be quite improbable to achieve the 1:1 Voronoi foam structure if the nanograins coarsening follows the standard von Neumann curvature-driven grain growth theory [35,36]. Here we believe the carbon spheres in our process are essential in providing the long-range director (purple arrows in Fig. 6a) for 1:1 arrangement, by the following mechanisms:

i) The green body contains a lot of nanopores at the rough contact interfaces between coated spheres. Elimination of these nanopores is energetically more urgent than nanograins coarsening, because surface energy is higher than grain boundary energy. In usual sintering without pressure, the nanopores can easily coarsen into some very large pores inside the material, which degrade the performance. Here, however, the initial carbon spheres are porous themselves, and provide natural sink for the excess vacancies emitted from these "contact nanopores" at the rough contact interfaces.
ii) Due to this initial radial flux of vacancies from outside the "circle of influence" to the central carbon sphere, grain growth inside the "circle of influence" is greatly expedited. The standard grain growth theory [35,36] requires grain boundary migration and short-range diffusion only. But here, the long-range vacancy influx (purple arrows in Fig. 6a, percolating through the nanograin boundary network) like drainage basin in hydrology would greatly accelerate grain boundary migration and grain coarsening within the sphere of influence, before the contact nanopores at rough contact interfaces are completely eliminated and two spheres start to compete for atoms.
iii) By the time the rough contact interfaces are eliminated completely (Fig. 6e), it is likely that the 1:1 arrangement have already formed completely (a single grain has already unified each and every "circle of influence", as demonstrated in Fig. 6c). Thereafter, grain coarsening would be a much slower process, because with the high uniformity of the coated spheres, the ceramic grains are all of nearly equal sizes.
iv) The green body will then slowly undergo about 40% volume shrinkage, due to the elimination of free volume accumulated in each carbon sphere (one can think of this process as pore coarsening, with the free space outside of the sample being by far the largest "pore"). In other words, the carbon spheres will shrink, with the ones closest to the sample free surface shrinking the fastest. However, during the 1650 °C sintering in Ar protective environment, the carbon cannot disappear, so there is a limit to how much the carbon sphere can be squeezed. One can reduce, but never eliminate, the center space extended by the densified carbon. After waiting for considerable time (due to slowness of (c), one can afford to wait a long time), all the carbon spheres are fully squeezed, and one achieves beautiful Voronoi tessellation with close-to-perfect tetrakaidecahedron shaped grains.
v) Then in the last step of 800 °C oxygen exposure, one eliminates the carbon spheres, and ends up with a highly monodisperse Voronoi foam with nearly identical grain and pore sizes, essential to the excellent thermal stability of the final product.

Conclusions

In summary, the hollow-grained $La_2Zr_2O_7$ "Voronoi Nanofoam" with ultralow thermal conductivity, sufficient mechanical strength and excellent thermal stability in air across a wide temperature range has potential as thermal insulation and corrosion protection layer in energy, aerospace, manufacturing, and microelectronics industries, where the challenging mechanical environment (such as erosion) and/or high temperature makes aerogels impractical. Our approach of making these nanoporous ceramics in bulk form is very general, and should apply to a wide variety of ceramics besides $La_2Zr_2O_7$. The results demonstrate the unique properties of cellular ceramics where a macro property can be tuned by orders of magnitude, while still maintaining the extraordinary thermal and corrosion stabilities of crystalline ceramics. It firmly demonstrates the rationale and power of nanotechnology for high-temperature applications, by design.

Declaration of Competing Interest

The authors declare that they have no known competing financial interests or personal relationships that could have appeared to influence the work reported in this paper.

Please cite this article in press as: S. Li et al., Materials Today (2021), https://doi.org/10.1016/j.mattod.2021.02.003

Acknowledgments

The authors would like to thank the financial support from the National Natural Science Foundation of China (NSFC–No. 51872159, 51172119, 90816019 and 11232008). JL acknowledges support by NSF CMMI-1922206.

Data availability

All data needed to evaluate the conclusions in the paper are present in the paper and/or the Supplementary Materials. Additional data related to this paper may be requested from the authors.

Appendix A. Supplementary data

Supplementary data to this article can be found online at https://doi.org/10.1016/j.mattod.2021.02.003.

References

[1] H. Gao et al., P. Natl. Acad. Sci. USA 100 (2003) 5597–5600.
[2] L.R. Meza et al., Science 345 (2014) 1322–1326.
[3] P. Colombo, Science 322 (2008) 381–383.
[4] L.J. Gibson et al., Cellular Solids: Structure and Properties, Pergamon Press, Oxford, 1989.
[5] X.W. Low et al., Adv. Mater. 20 (2008) 3987–4019.
[6] X. Wang et al., Chem. Rev. 116 (2016) 10983–11060.
[7] F. Hu et al., Adv. Mater. 31 (2019) 1801001.
[8] X. Zheng, Science 344 (6190) (2014) 1373–1377.
[9] R. Vassen et al., J. Am. Ceram. Soc. 83 (2000) 2023–2028.
[10] N.P. Padture et al., Science 296 (2002) 280–284.
[11] Y. Wang et al., Acta Mater. 68 (2014) 106–115.
[12] D.G. Cahill et al., Phys. Rev. B. 46 (1992) 6131–6140.
[13] S.G. Jennings, J. Aerosol. Sci. 19 (1988) 159–166.
[14] M. Knudsen, The Kinetic Theory Of Gases, 3rd ed., Wiley, New York, 1950.
[15] K.N. Tu et al., Appl. Phys. Lett. 86 (2005) 093111.
[16] X. Sun et al., Angew. Chem. Int. Ed. 43 (2004) 597–601.
[17] F.X. Zhang et al., Phys Rev Lett. 105 (2010) 015503.
[18] W. Xu et al., Int. J. Eng. Sci. 134 (2019) 31–46.
[19] A.Y. Smolin et al., Part.-Based Meth. II – Fund. Appl. (2011) 249–255.
[20] J.A. Cape et al., J. Appl. Phys. 34 (1963) 1909–1913.
[21] P. Ruckdeschel et al., Nanoscale. 7 (2015) 10059–10070.
[22] R. C.Weast, RC Press, Cleveland, Ohio, 1974.
[23] Z. Hashin et al., J. Appl. Phys. 33 (1962) 3125–3131.
[24] J.K. Carson et al., Int. J. Heat Mass Tran. 48 (2005) 2150–2158.
[25] C. Wan et al., Acta Mater. 58 (2010) 6166–6172.
[26] C.J. Durrant, Verlag Adam Hilger, Bristol and Philadelphia (1988).
[27] E. Litovsky et al., J. Am. Ceram. Soc. 79 (1996) 1366–1376.
[28] A.M. Limarga et al., Appl. Phys. Lett. 98 (2011) 211906.
[29] M.F. Ashby, Philos. Tran. Royal Soc. A: Math. Phys. Eng. Sci. 364 (2006) 15–30.
[30] C. Mougel et al., Polymer 164 (2019) 86–117.
[31] Y. Si et al., Sci. Adv. 4 (2018) eaas8925.
[32] T.A. Schaedler et al., Science. 334 (2011) 962–965.
[33] T. Liu et al., IOP Conf. Series: Mater. Sci. Eng. 490 (2019) 032033.
[34] N.G. Dou et al., Nano Lett. 18 (2018) 4755–4761.
[35] W.W. Mullins, J. Appl. Phys. 27 (1956) 900–904.
[36] R.D. MacPherson et al., Nature. 446 (2007) 1053–1055.

Please cite this article in press as: S. Li et al., Materials Today (2021), https://doi.org/10.1016/j.mattod.2021.02.003